

# Anomaly detection and automatic labeling for solar cell quality inspection based on Generative Adversarial Network

Julen Balzategui<sup>\*1</sup>, Luka Eciolaza<sup>1</sup>, and Daniel Maestro-Watson<sup>1</sup>

<sup>1</sup>Mondragon Unibertsitatea, Goiru Kalea, Arrasate/Mondragon, Spain  
 $\{jbalzategui, leciolaza, dmaestro\}@mondragon.edu$

## Abstract

In this manuscript, a pipeline to develop an inspection system for defect detection of solar cells is proposed. The pipeline is divided into two phases: In the first phase, a Generative Adversarial Network (GAN) employed in the medical domain for anomaly detection is adapted for inspection improving the detection rate and reducing the processing rates. This initial approach allows obtaining a model that does not require defective samples for training and can start detecting and location anomaly cells from the very beginning of a new production line. Then, in a second stage, as defective samples arise, they will be automatically labeled at pixel-level with the trained model and employed for supervised training of a second model. The experimental results show that the use of such automatically generated labels can improve the detection rates with respect to the anomaly detection model and the model trained on manual labels made by experts.

**Keywords**— Anomaly detection, Electroluminescence, Solar cells, Neural Networks

## 1 Introduction

In the last decade, about 2.6 trillion dollars have been invested in renewable energies, half of it in solar energy, with the objective of developing efficient alternatives to traditional energy sources such as oil or

gas (BNEF, 2019). The development of the technology has reduced solar electricity generation cost per kilowatt-hour by 81%. This cost reduction has turned the solar energy into an attractive source of energy for electricity production, increasing the installation of Photovoltaic (PV) cells by 36.8% between 2010 and 2018 (BNEF, 2019). It is expected that this investment trend will remain in the following years (IEA, 2019).

During the assembly of the panels, different events, such as excessive mechanical stress on the panel or a soldering failure, can lead to defects that can harm the long-term energy generation capacity of the module. A defect that covers the 8% of the total cell area may not have a significant impact on the performance if the cell is isolated. However, the same area can have a significant impact when cells are connected and soldered to each other in cell arrays (Köntges et al., 2011) which is the common layout. In the future, the defective area may spread, breaking the cell and considerably reducing the energy production capacity of the module. As the production increases, the quality inspection becomes critical to avoid defective cells being assembled into the final panel, and thus, to ensure high efficiency and reliable performance of the produced panels.

Nowadays, different imaging techniques are used during PV module inspection to obtain images where defects appear highlighted, for example, Electroluminescence (EL) (Bartler et al. (2018), Chen et al. (2020)), Photoluminescence (PL) (Demant

---

<sup>\*</sup>Corresponding author

et al. (2016), Nos et al. (2016)), or Thermography (Pierdicca et al. (2018), Vaněk et al. (2016)). In industrial scenarios, the EL is one of the predominant techniques. In EL, the cells emit light under electrical current by the phenomenon of electroluminescence. This light is then captured in high-resolution images where defective areas, with less current flow, appear darker than the remaining parts of the cell (Fuyuki and Kitayanan, 2009). The most common defects that may arise are cracks, breaks, and finger interruptions (Tang et al., 2020). Fig.1 shows the appearance of these kinds of defects in EL images. This technique requires high control over the environmental conditions since the images have to be taken in total darkness. While this requirement makes EL unfeasible for the inspection of outdoor installed panels, it can be used to obtain high-resolution images with highlighted defects during the assembly phase.

Despite these enhanced images, the defect detection process has still to be done by checking each of the cells individually. This process is currently done to a great extent by human operators, who are prone to error as it is hard for humans to meet the industrial production cycle time. For example, a panel composed of 60 PV modules must be examined in under 30 seconds, which means half a second for each module. Also, human subjectivity is inevitable when deciding if a cell is defective or not, affecting the quality inspection effectiveness. In recent years, several proposals have been made towards the automation of quality inspection. By automating the inspection, all the cells can be checked faster and always using the same objective criteria, overcoming the previous limitations.

The proposed approaches for automatic PV module inspection can be grouped into three categories according to the required level of human intervention: 1) traditional image processing based approaches, where the procedures used to highlight and binarize defective areas in the images must be manually defined, 2) shallow learning approaches, where machine learning techniques are used for defect identification based on meaningful features that must be obtained through manual feature engineering, and 3) Deep learning techniques, where the features are automatically obtained from the data. Note that higher

levels of human intervention in the image processing algorithm development imply larger and more complex changes in the system in order to adapt to new requirements.

The remainder of the paper is organized as follows: Section 2 presents some background and related works in the field of photovoltaic cell inspection. In section 3, the unsupervised and supervised training stages are explained. In sec.4 the different experiments, the employed dataset and the used metrics are detailed. In section 5 the results from the experiments are described. Finally, in section 5, some conclusions are provided.

## 2 Related works

In this section, some of the proposed approaches for the automatic detection of defects in images of PV modules are going to be summarized.

The traditional image processing methods are mainly based on manual feature engineering. In this process, the discriminating characteristics of the defects are used to process and binarize the images to highlight the defects. For example, using Anisotropic diffusion filter (Ko and Rheem (2010), Anwar and Abdullah (2014)) or modified steerable filters ((Chen et al., 2019), (Chen et al., 2018b)), the background in the modules are smoothed thus only defects remain. Or inversely, apply Anisotropic diffusion (Tsai et al., 2010) or filters in frequency domain (Tsai et al., 2012) to remove the defects in the cells, so then the difference between the filtered and the original image is used to highlight the defects.

In other works, the manual feature extraction is combined with shallow learning methods: In (Tsai et al., 2013) and (Zhang et al., 2013), they extract Independent Component Analysis basis (ICA) from defect-free solar cells samples to construct a demixing matrix. At the inspection stage, the images are reconstructed using the learned basis images and the reconstruction error is used for detecting the presence of defects. In Rodriguez et al. (2020), 20 different LoG-Gabor Filters are used to extract 81 features for each pixel in the images. Then, the Principal Component Analysis (PCA) is used to refine these

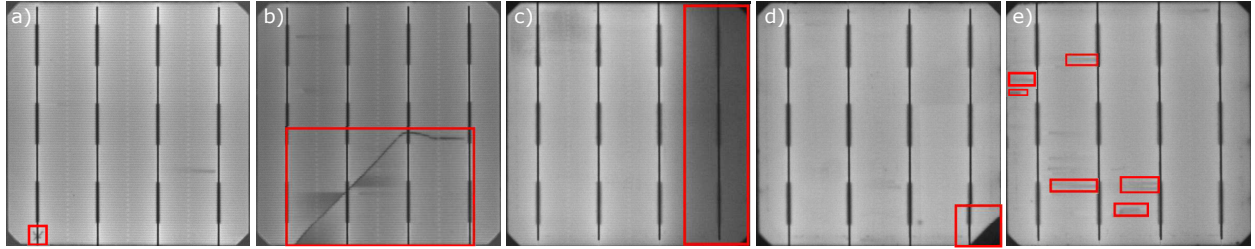


Figure 1: Different type of defects highlighted in Electroluminescence images of solar cells. The defects are: a) microcrack, b) crack, c) bad soldering, d) break and e) finger interruptions

features, and finally, a Random Forest model classifies each pixel into a non-defective or defective. In (Tsai et al., 2015), they extract characteristics of local grains patterns and clusterize them using Fuzzy C-means. At testing stage, the distance of the grains from the samples to the clusters is used to decide if a grain is defective or not. Similarly in (Su et al., 2019), they use a modified Center-Symmetric Local Binary Patterns (CS-LBP) feature descriptor to extract features from the defective areas in the cells, which are then used to train the K-means algorithm. The cluster centroids from training samples are employed to generate global feature vectors to train a classification algorithm, such as the Support Vector Machine (SVM).

Overall, both traditional image processing methods and traditional methods in combination with shallow machine learning techniques can achieve high defect detection rates. However, the manual feature engineering is usually time-consuming and requires high domain knowledge. In addition, inspection systems based on these approaches are commonly very case-specific solutions which lack adaptability. A change in the data can mean a substantial change in the inspection system, which would require additional time-consuming manual feature engineering labor to adapt it.

In more recent works, Deep Learning methods have been widely applied for the solar cell inspection field. These methods, can directly extract meaningful features from the raw data without any feature engineering work, thus making these methods more flexible to changes. The following works (Bartler et al.

(2018), Ying et al. (2018), Sun et al. (2017), Akram et al. (2019), Dunderdale et al. (2020), Deitsch et al. (2019), Akram et al. (2020), Chen et al. (2018a), Chen et al. (2018a)) are some examples of how Convolutional Neural Networks (CNN) have been employed for classifying solar cells as defective or defect-free during the quality inspection with accuracy rates above 88.2%. In addition to a classification, in some cases the location of the defects in the cells is also provided which improves the results interpretation, for example, by a explicit segmentation (Balzategui et al. (2020), Rahman et al. (2019)), using bounding boxes (Liu et al. (2019), Zhang et al. (2020)), or by visualizing the activation maps from the last network layer (Deitsch et al. (2019), Mayr et al. (2019)). Nevertheless, to obtain high detection rates, the networks are trained using supervised learning, which requires a considerable amount of annotated defective data. The quality of the results (i.e. detection rate) in supervised learning is directly proportional to the amount of employed annotated data. However this represents a challenge in many industrial applications as sufficient defective samples may be difficult to obtain in an industrial setting. Thus, the creation of accurate inspection models may be difficult, as a new manufacturing line will need time to generate a representative database with enough examples. There may also be certain very rare defect types.

To tackle the problem of insufficient defective data, several researchers have proposed different solutions: one of the approaches is transfer learning (Akram et al. (2020), Demirci et al. (2019), Qian et al.

(2020a)), where the neural network is initialized using weights from a previously trained network. Then, the model is refined using few case specific samples. Transfer learning is limited by the similarity between the source and target domains. Nowadays, the available pre-trained weights have been mainly trained on natural images rather than on industrial datasets, which can limit their use in industrial cases.

Another proposed approach consists in generating synthetic data to compensate imbalanced datasets (Tang et al. (2020), Luo et al. (2019), Wang et al. (2019)). In these works, they employ variants of the Generative Adversarial Network (GAN) (Goodfellow et al., 2014) to learn latent features from defective samples. Then the latent space is used to generate synthetic defective samples that are employed along with real samples to train a final CNN. Nonetheless, both Transfer Learning and GANs, still require defective data.

To avoid the need of defective data, other researchers have used the anomaly detection approach. The objective in this approach is to train a network to learn the features that characterize normal samples. Then, the learned features can be used to discriminate samples that will be far from what is considered normal, and thus, detect defective samples. In anomaly detection, just defect-free samples are used during training and there is no need for annotations. These features make the anomaly detection an interesting approach for industrial applications. Anomaly detection has been applied in different industrial cases, e.g. (Haselmann et al., 2018), (Staar et al., 2019) and also the medical domain, e.g. (Schlegl et al., 2019), (Chen and Konukoglu, 2018), where it is also difficult to obtain anomalous data for training.

In the case of solar cell inspection, in (Qian et al., 2020b) and (Qian et al., 2020a) they propose to train a Stacked Denoising AutoEncoder (SDAE) to extract features from defect-free samples using the sliding window method. In (Qian et al., 2020a), they extend the network architecture with a pre-trained VGG16 network that works as additional feature extractor. This extra branch extracts additional features which are then fused with the already extracted feature maps enhancing the obtained information. At testing

time, the same procedure is applied but on defective samples. The extracted features are then processed using matrix decomposition to localize the defects in the cells. After that, some morphological processing is applied to improve the results. However, in these works, only crack type of defect detection is targeted. Furthermore, the images are processed using the sliding window method. This procedure slows down the inspection process limiting its deployment into a real production environment.

In this work, we propose a pipeline for monocrystalline solar cell quality inspection. The pipeline is based on anomaly detection approach. The pipeline is structured in two phases:

- First, f-AnoGAN proposed (Schlegl et al., 2019) is modified to adapt it for inspection. Instead of processing the images using the sliding window method, now the images are processed as a whole, which reduces the processing time. Also, the training scheme is altered which has resulted in an improvement in the defect detection rate with respect to the results with the original training scheme. This network will act as anomaly detector, which in experiments have shown that is able to detect and locate different types of defects such as crack, microcracks or finger interruptions.
- Second, the segmentation results from the anomaly detection model are used as automatic pixel-wise labels in a supervised model training to improve defect location results.

The proposed procedure allows obtaining an initial inspection model that can detect and locate anomalies in the cells from the very beginning using just defect-free cell samples. Then, as defective cells arise, the model will separate them from the defect-free ones and output pixel-level annotations without human intervention. When enough annotated defective cell samples are accumulated, a more accurate supervised defect detection and localization model will be developed. Automatically annotated images prove to train more precise models compared to manually annotated images.

### 3 Methodology

This section details how the different networks in the pipeline are trained. The general scheme of the pipeline is shown in Fig.2. The training is performed in the first and third steps exhibited in the image.

#### 3.1 Unsupervised training

f-AnoGAN is composed of three different subnetworks: a generator, a discriminator, and an encoder, which are trained in two different phases. First, the generator and discriminator are trained in an adversarial manner to learn a latent space of normal data variability using just normal data. In this work, defect-free samples are considered as normal data and defective samples as abnormal data.

After the first stage, the two networks are kept unaltered while the encoder is trained to map normal data from the image space to learned latent space. Once these two phases have finished, the encoder can map test images from the image space to the latent space, and the generator can reconstruct the encoded version of the images from the latent space back to the image space. Finally, the deviation between the original image and the reconstructed version of that image is used for anomaly detection and location.

##### 3.1.1 Phase 1 - WGAN training

The objective of the first phase consists in learning the variability of normal data. For this purpose, a Wasserstein GAN (WGAN), composed by a generator and a discriminator, is optimized to learn the normal data probability distribution. The optimization is achieved using gradient penalty based loss shown in eq.1 proposed by (Gulrajani et al., 2017), where the Wasserstein distance between the real normal data probability distribution  $P_r$ , and generator synthesized data probability distribution  $P_g$  is minimized.

$$L_{WGAN} = \mathbb{E}_{\tilde{x} \sim \mathbb{P}_g} [D(\tilde{x})] - \mathbb{E}_{x \sim \mathbb{P}_r} [D(x)] + \lambda \mathbb{E}_{\hat{x} \sim \mathbb{P}_{\hat{x}}} [\|\nabla_{\hat{x}}(D(\hat{x}))\|_2 - 1]^2 \quad (1)$$

where  $\tilde{x} = G(z)$ ,  $\hat{x} = \alpha x + (1-\alpha)\tilde{x}$  with  $\alpha \sim U(0, 1)$  and  $\lambda$  is the penalty coefficient. During the training, the generator is fed with a noise input vector  $z$ , sampled from a latent space  $Z$ , and tries to learn the mapping from that latent space to the image space  $X$ . The synthesized data  $G(z)$  should follow as close as possible the real data distribution  $P_r$ . Simultaneously, the discriminator is given the generated sample  $\tilde{x}$  and the real sample  $x$  so it outputs a scalar about how close both distributions are.

After the first phase of the training, 1) a latent space that represents the variability of the normal data, 2) a generator that can map samples from this latent space to image space, and 3) a discriminator that can detect samples that do not follow the normal data distribution are obtained.

However, at this stage the network has not learned the inverse mapping, i.e. from image space to latent space. By learning the inverse mapping, it would be straightforward to obtain the reconstruction of the image, and thus, speed up the anomaly detection process. In a second training phase, this mapping is learned.

##### 3.1.2 Phase 2 - encoder training

In the second training phase, an encoder is trained along with the generator and discriminator from the previous stage. The objective at this stage is to make the encoder learn to map a real image to the latent space such that the generator can map it back to the image space. During this stage, both the generator's and the discriminator's weights are fixed so they remain unaltered during the training. This network configuration is denoted as *izi* in (Schlegl et al., 2019). In this case, the encoder is optimized by minimizing the Mean Square Error (MSE) with the respect to the difference between the original image  $x$  and the reconstructed one  $G(E(x))$ . Additionally, the reconstruction error from the *izi* architecture loss is extended by feature residuals from an intermediate layer in the discriminator yielding the *izi<sub>f</sub>* architecture. By taking into account these residuals in the feature space, the reconstruction is improved (Schlegl et al., 2019). The final loss function of *izi<sub>f</sub>* is defined

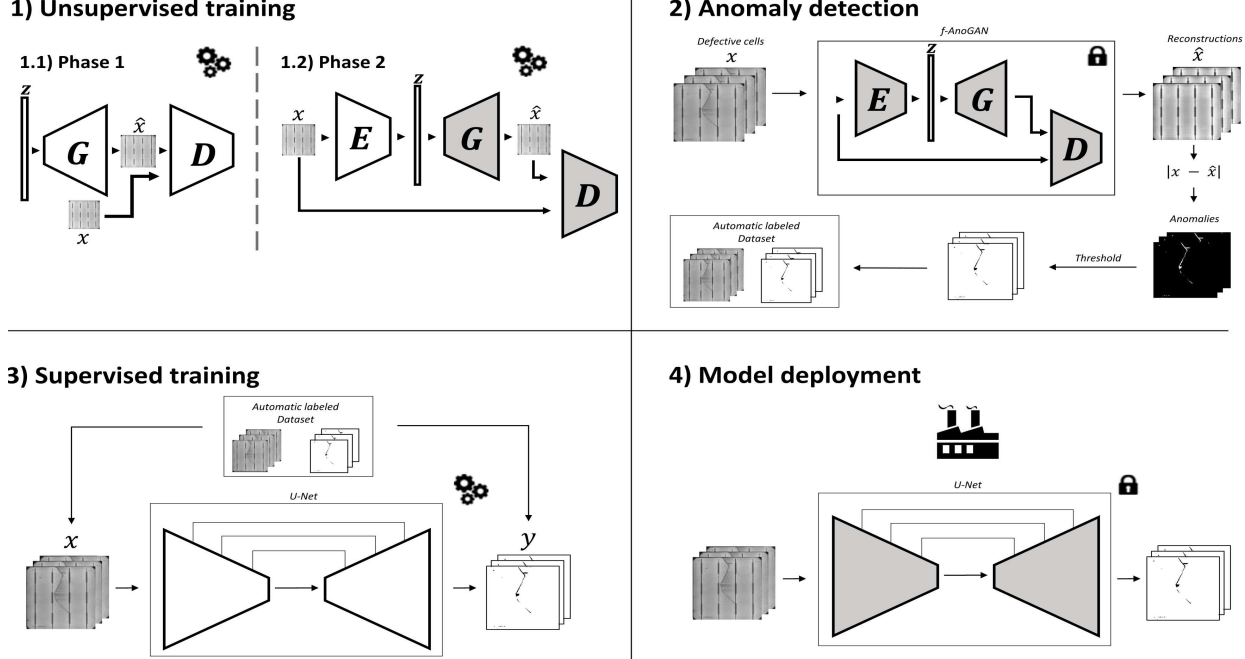


Figure 2: General schema of the proposed pipeline. 1) In the unsupervised training, the network for anomaly detection is trained. 2) In the anomaly detection, the network from the previous step is applied to detect and locate defects, and thus, generate automatic labeled dataset. 3) The generated dataset is employed to train a supervised model. 4) After the supervised training, the model is ready for deployment. The lock and gears represent when the model is not being trained and when it is, respectively

by eq.2:

$$L_{izi_f} = \frac{1}{n} \|x - G(E(x))\|_2 + \frac{k}{n_d} \|f(x) - f(G(E(x)))\|_2 \quad (2)$$

where  $f(\cdot)$  are discriminator's intermediate layer features,  $n_d$  is the dimensionality of the intermediate feature representation, and  $k$  is a weighting factor.

### 3.1.3 Anomaly detection

Once the training has finished, all the components are fixed and ready to be used for anomaly detection. During the detection, the images are processed as in the encoder training. First, the encoder maps the images to the latent space, and then, the generator maps them back to the image space. Finally, the difference between the reconstructed and the original

image defined in eq.3 is used for anomaly detection. This process is reflected as the second step in fig.2.

$$A(x) = A_R(x) + k \cdot A_D(x) \quad (3)$$

where  $A_R(x) = \frac{1}{n} \|x - G(E(x))\|_2$ ,  $A_D(x) = \frac{1}{n_d} \|f(x) - f(G(E(x)))\|_2$  and  $k$  is a weighting factor from eq.2.

As just defect-free cell samples have been used for training, the network will have only learned to reconstruct normal samples. Fig.3, shows how the network acts when projecting defect-free and defective sample images to the learned latent space, and how the images are reconstructed back. In the case of defect-free sample, the network outputs a similar image as the the input image, thus there is not much deviation when subtracting one image from the other. Instead, when processing a defective cell, it outputs

a defect-free version of the input sample. As a consequence, the deviation between the original and the reconstructed images will be much larger.

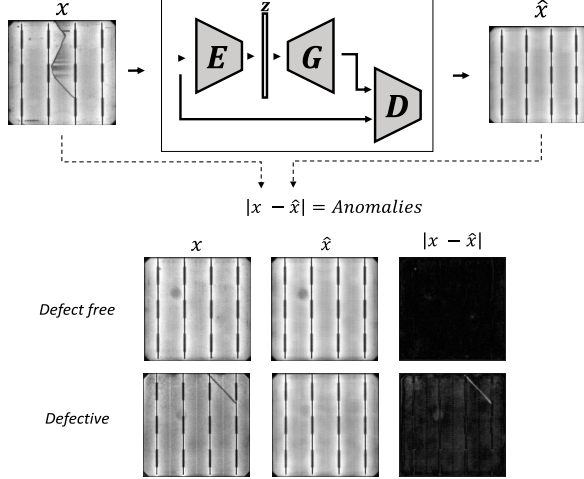


Figure 3: Example anomaly detection with f-AnoGAN with defect free and defective cell samples.

Moreover, the absolute value of the pixel-wise difference between the original and the reconstructed image,  $|x - G(E(x))|$ , is used for pixel-wise anomaly detection. By applying a threshold  $c$ , defined in eq.4, to the residuals image obtained from  $|x - G(E(x))|$ , the binary image  $y \in \{0, 1\}$  is obtained.

$$y = \begin{cases} 1, & c \geq |x - G(E(x))| \\ 0, & \text{otherwise.} \end{cases} \quad (4)$$

This binary image can be considered as pixel-wise label of defective samples as described in sec.3.2.

### 3.1.4 Modifications

In this work, two modifications have been made over the original f-AnoGAN network to adapt it for anomaly detection in photovoltaic cell manufacturing. With f-AnoGAN, the images are processed in patches of size 64x64 pixels, which increases the time to process a entire cell. As a consequence, the network does not meet the industrial production cycle time (under one second per cell). In order to reduce

the inspection time, the encoder input and the generator output layers' dimension was modified. In f-AnoGAN, these layers are fully connected layers that have 8196 units. The modification consists in increasing dimension to 65536 units, such that the network can handle a resized image of 256x256 pixels. With this resolution, the smallest defects will remain in the images and the images will be processed in a single step meeting the specified inspection time. Also, the number of kernels from the convolutional layers in the network was reduced to avoid overfitting. The original kernel sequence of 512-256-128-64 in the encoder, and the inverse in the decoder, was halved to 256-128-64-32. Several experiments were done with higher resolution images, however, the results were not successful.

Moreover, the training scheme was also modified. In f-AnoGAN, the generator is frozen during the second training phase in sec.3.1.2, thus, only encoder weights are modified. This can limit the network capability in terms of reconstructing the input image. In other works, e.g. (Akcay et al., 2019), all network components are trained at the same time, which does not impose any kind of limitations on the network. However, the phase based training where some modules are kept unaltered can be important for network training stability. Therefore, instead of using a single phase training scheme and train all the network components at the same time, an intermediate solution was chosen. In order to maintain a stable training without restricting the reconstruction capability, the generator is also trained at certain number of the encoder training iterations with a learning rate of 1e-4 and 5e-5 for the encoder and generator, respectively, while keeping the discriminator unaltered. By training the generator, the reconstruction of defect-free samples will improve, therefore, the deviation between the original and the reconstructed images of normal data will be reduced. Consequently, both the anomaly score and the pixel differences will be low for defect-free samples, but high for defective ones, thus the model's detection rate will improve.

## 3.2 Supervised training

After obtaining a defect location with anomaly detection, these results can be considered as pixel-wise annotation proposals and could be used for supervised training. In this way, a more accurate model regarding defect location and detection can be achieved. Thus, it will not be required to spend time on the time-consuming data annotation task.

In a supervised training, the model is specified using labels to search for specific defective patterns in the data. Instead, in anomaly detection the model is taught to find everything that is not considered normal. Because of this, supervised learning usually yields more precise models for defect detection than using anomaly detection. Nevertheless, anomaly detection can be used to obtain pixel-wise labels without requiring any human intervention. In this way, in the first stage of the inspection system development, where lots of defect-free cell samples and few defective cell samples are available, an initial inspection model can be obtained using anomaly detection. Then, as defective cells arise, the trained model will process the samples and output pixel-wise annotations. After some time, when there are enough annotated defective cells samples, supervised learning can be used to obtain a model that yields more precise results.

For the supervised training U-net (Ronneberger et al., 2015), an end-to-end trainable Fully Convolutional Neural Network (FCN) architecture that has shown to work well on biomedical image segmentation with low amounts of data, was used. The network is composed of two sequential parts: an encoder and a decoder. In the encoder, convolutional layers are grouped in blocks that extract features from the data while they are downsampled in consecutive steps to facilitate the extraction. Then in the decoder, the low-resolution features are transformed into a final segmentation map by successive upsampling steps. During the downsampling process, localization information is lost. In order to recover that information, skip connections are used between encoder and decoder blocks in the upsampling process.

The network is trained to minimize the difference between the output and the pixel-wise annotation

that works as ground truth. In this training, the optimization is done using the dice loss eq.5.

$$L_{dice} = -\frac{2 * \sum_j p_j g_j}{\sum_j p_j + g_j} \quad (5)$$

where  $p \in [0, 1]$  is the network output, and  $g \in \{0, 1\}$  is the ground truth.

## 4 Evaluation

In this section, the experiments that have been carried out, the dataset that has been employed, and how the results have been analyzed will be explained.

### 4.1 Experiments

For this manuscript, several experiments have been performed regarding the unsupervised training and the supervised training. In the unsupervised training, the defect detection rates between f-AnoGAN and f-AnoGAN with the proposed modifications are compared. In the supervised training, the defect localization precision between a model trained with manually annotated samples and a model trained with automatically annotated samples is compared.

#### 4.1.1 Unsupervised training

For the first experiment, the detection rate of f-AnoGAN is measured against the detection rate of f-AnoGAN with the architecture modification. This experiment aimed to compare the detection rate and the time required to process the images between the patch-based approach and approach where the images are processed in one step. The models in this experiment will be referred to as f-AnoGAN-64 and f-AnoGAN-256, respectively.

The hyperparameters for the two models were all kept the same as in (Schlegl et al., 2019): The  $z$  vector was sampled from a Normal distribution and had a size of 128, the value of  $\lambda$  parameter for the gradient penalty was 10, and the value for the weighting factor  $k$  in eq.2 was set to 1. The optimization algorithm for the first training phase was Adam (Kingma and Ba, 2014) and for the second RMSprop (Hinton et al.,

2012). Regarding the training of these models, they took a different number of iterations depending on the phase and approach. For f-AnoGAN-64, the network is trained during 40k iterations in the first phase and 70k iterations in the second phase with a batch size of 64 images. In f-AnoGAN-256, the first training phase took 40k iterations and the second phase required 50k iterations. The architecture modification in f-AnoGAN-256 increased the total number of parameters of the network which also increased the memory requirement to train the model. In order to fit the model in memory during training, the batch size was reduced to 14.

After the first experiment, the training scheme of f-AnoGAN-64 and f-AnoGAN-256 models was altered in a second experiment. This second experiment aimed to check if the training scheme modification could improve the final defect detection rate. The network architecture, hyperparameters, and image processing procedures were kept the same as in f-AnoGAN-64 and f-AnoGAN-256, just the training scheme was altered. These new two models will be referred to as f-AnoGAN-64\* and f-AnoGAN-256\*. When considering the generator in the second phase of the unsupervised training, more iterations were required until the models converged. For f-AnoGAN-64\*, 100k iterations were required, and for f-AnoGAN-256\* 70k iterations were needed.

In addition to all the models from the previous experiments, two Convolutional Deep Autoencoders were also trained. These models served as a base comparison and were used to check if a simple network architecture could obtain high defect detection rates. Following the two approaches to process the images in the previous experiments, one Autoencoder was trained to process the images in patches, and the other Autoencoder was trained to process the images in one step. These models will be referred to as AE-64 and AE-256. Regarding the architectures, both networks are composed with an encoder and a decoder with several convolutional layers. In the case of AE-64, the encoder has two convolutional layers with 64-32 filter distribution, then 4 Fully Connected layer of 16 units each, and finally a decoder with the inverted shape of the encoder part. In the case of AE-256, the architecture is two convolutional layer

deeper than the AE-64 so the output dimension before the Fully Connected layer is the same. The filter distribution is 8-16-32-64.

After each Fully Connected layer, a dropout layer with a drop rate of 0.25 was set. Both networks were optimized with the MSE loss function and Adam as the optimization algorithm. The AE-64 model training took about 30k iterations with a batch size of 32, and the AE-256 model training took about 6k iterations with a batch size of 8.

#### 4.1.2 Supervised training

After the unsupervised training, a Fully Convolutional Network was trained using the labels obtained from the anomaly detection results. In this experiment, the segmentation results from a model training on automatic labels and a model trained with labels annotated by experts were compared. The goal of this experiment was to prove the feasibility of using the anomaly detection approach as an automatic labeling method. Precise segmentation results using these automatic labels will avoid spending time on the time-consuming and not always trivial pixel-level labeling task. In this way, it will considerably reduce the time required for a new inspection system setup.

For both manual and automatic labeling models, U-net (Ronneberger et al., 2015), an end-to-end trainable FCN, was used. The network configuration was kept the same as in (Ronneberger et al., 2015), which is composed of 9 blocks of convolutional layers: 4 in the encoder, 4 in the decoder, and a middle block that acts as a bottleneck. The networks were trained for 1000 iterations using Adam as the optimization algorithm.

## 4.2 Dataset

Regarding the dataset, a real industrial dataset composed of Electroluminescence images of 1873 monocrystalline solar cells extracted from 31 panels was employed. The images were provided by Mondragon Assembly S. Coop. and were taken at the quality inspection stage during the assembly of solar panels. The cells have a size of 15x15 cm and the images have an average resolution of 840x840 pixels.

In the dataset, there were 1498 defect-free cell images or the possible impurities the company did not consider severe enough to label them as defective. The remaining 375 were defective cells that contain cracks, microcracks, and finger interruptions. The defective samples were reserved only for the final evaluation. Instead, the defect-free samples were separated into train, validation, and test sets. The train and validation sets were used during the training phase, and the test set was put aside along with all defective samples for the final evaluation. The distribution of the dataset is shown in tab.1.

	<b>Train</b>	<b>Val</b>	<b>Test</b>	<b>Total</b>
<b>Defect-free</b>	750	373	375	1498
<b>Defective</b>	-	-	375	375
Crack	-	-	18	-
Microcrack	-	-	240	-
Finger interruptions	-	-	117	-

Table 1: Dataset sample distribution

Each defective sample has its manually labeled pixel-wise binary annotation  $\{0, 1\}$  of the same size as it is shown in fig.4.

The dataset was pre-processed in order to adapt it for the experiments. For the patch-based approach based models, the images were split into patches using the sliding window method. Before extracting the patches, every image was first increased to a resolution of 1024x1024 pixels, and then, 256 patches were extracted per image. The images were first resized so when extracting patches of size 64x64, there will be even fractions. This way it will not be necessary to overlap patches in order to process the entire cell. After extracting the patches, The final train, validation, and test sets were composed of a total of 192000, 95488, and 192000 (9600 defective and 9600 defect-free) images, respectively. For the other networks (f-AnoGAN-256, f-AnoGAN-256\* and AE256), the images were resized to 256x256 resolution. In all the experiments, the images were normalized so the values were in the range [-1,1].

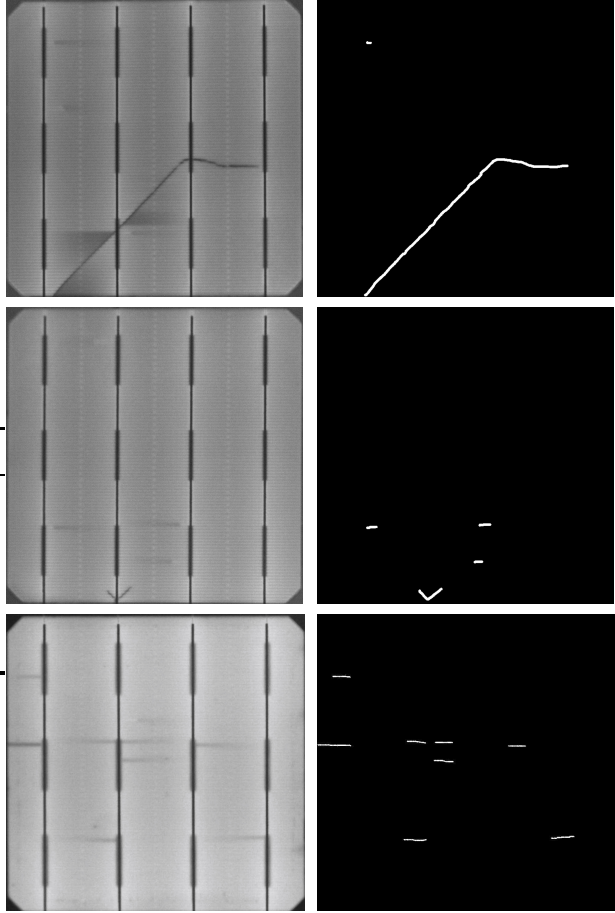


Figure 4: Defective monocrystalline samples with their pixel level annotations

### 4.3 Metrics

The results from the experiments were measured quantitatively and qualitatively. For the defect detection performance assessment in unsupervised experiments, the anomaly score from eq.2 was used in every image. Then, the scores were used to construct the Receiver Operating Characteristic (ROC) curves and to calculate the Area Under Curve (AUC). This is a widely used metric for binary classification problems, which describes how good the classifier is at discriminating one class (e.g. defective) from the other class (e.g. defect-free). An ideal classifier would obtain an

AUC of 1, while a random classifier would achieve a 0.5. Note that, to analyze the results per type of defect, there is a great unbalance between defective and defect-free samples tab.1. To avoid misleading conclusions when interpreting the ROC curve, the data was balanced by first taking all defective samples of the class that was being analyzed, and then, randomly selecting the same amount of defect-free samples. Based on the ROC curve, the Youden Index was taken to binarize the results and compute Precision, Recall, Specificity, and F1-score metrics, defined in eq.6,7,8, and 9 respectively. The results for these metrics are shown in tab.2.

$$Precision = \frac{TP}{TP + FP} \quad (6)$$

$$Recall = \frac{TP}{TP + FN} \quad (7)$$

$$Specificity = \frac{TN}{TN + FP} \quad (8)$$

$$F1-score = 2 \cdot \frac{Precision \cdot Recall}{Precision + Recall} \quad (9)$$

where TP stands for True Positive, TN for True Negative, FN for False Negative and FP for False Positive.

To compare the performance between the models, the results from the patch-based approaches were post-processed. While in the f-AnoGAN-256, f-AnoGAN-256\*, and AE-256 it is enough to apply a threshold to evaluate a cell as defective or not, in patch-based approaches the errors of all patches must be taken into account. In this case, the same threshold was applied to every patch. Then, the number of patches evaluated as defective was counted. Based on the number of defective patches, the whole cell was evaluated as defective or non-defective. In the employed dataset, the smallest defects are smaller than a patch. As there is no overlap between patches when processing the images, if a single patch was evaluated as defective, the entire cell was also evaluated as defective.

For the experiment in the supervised part, the 375 defective cell images were employed. The images were distributed as 340 for training and the remaining 35 for testing (2 crack images, 20 microcrack images

and 12 finger interruptions images). As there were few samples left for testing, the performance of the models was mainly evaluated at a qualitative level. Despite that, the performance at pixel-level pixels has been also reported with mean Intersection Over Union (mIoU) defined in eq.10.

$$IoU = \frac{TP}{TP + FP + FN} \quad (10)$$

#### 4.4 Experimental setup

Regarding the hardware and software specifications: Two Nvidia GeForce RTX 2080 GPUs were used in the experiments. The models' training in the unsupervised part required both GPUs, while the anomaly detection and supervised training only required one GPU. For all f-AnoGAN based models the code in [github:f-AnoGAN](https://github.com/zhongyuanli/f-AnoGAN) was used, which is written in Python2.7 and employs Tensorflow 1.2 and CUDA 8. Instead, in the Convolutional Deep Autoencoder and supervised U-net training, Python 3.6, Tensorflow 1.14, and CUDA 10 were used.

## 5 Results

In this section, the results from the experiments in unsupervised part and supervised part are presented. The results are going to be analyzed by the experiments described in sec.4. However, to ease the results comparison between the models, all the results are shown together in fig.5, fig.6 and tab.2.

### 5.1 Patch wise vs. image wise

This first experiment sought to check how the modification of the architecture would affect the detection rate of the network and the time needed to process the images.

The results from the model where the architecture was modified (f-AnoGAN-64 → f-AnoGAN-256) showed an improvement in the precision metric. It can be observed in tab.2 that f-AnoGAN-256 obtained greater precision and specificity values but lower recall value than f-AnoGAN-64. This means that with the architecture modification, the network

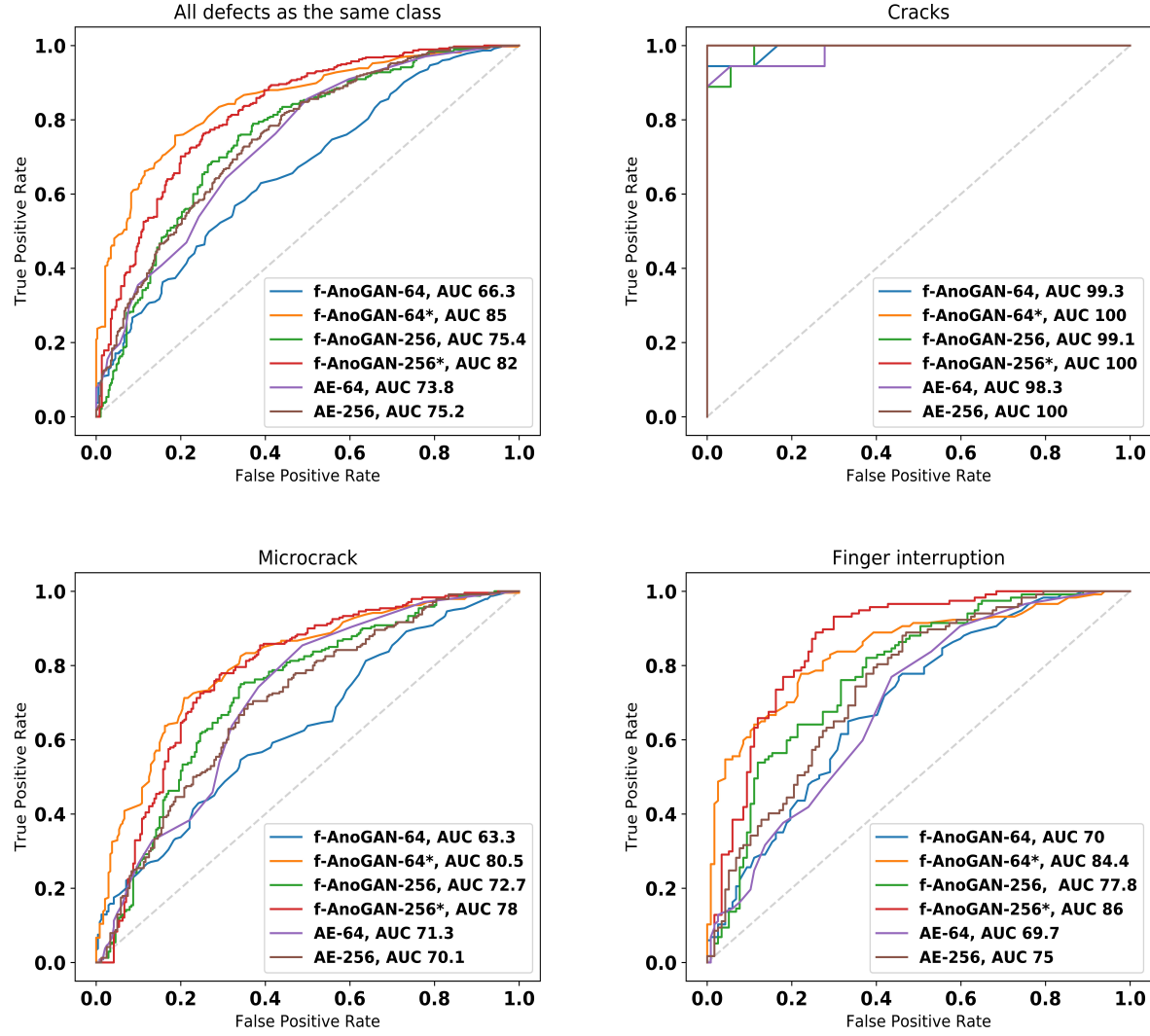


Figure 5: ROC curves from the different experiments

had less false positive cases, in other words, it was more precise when classifying defective cells than f-AnoGAN-64. However, less defective cases were detected.

If the results from f-AnoGAN-64 and f-AnoGAN-256 are compared with the results from Convolutional Deep Autoencoders, it can be seen that there was not

an improvement in the detection rate. Despite performing better on finger interruption type of defect, both f-AnoGAN based models obtained overall worse detection rates than their Autoencoder counterparts, i.e. AE-64 and AE-256. Additionally, a visible difference can be observed in the results when comparing the two approaches to process the images. In gen-

Model	AUC	Precision	Recall	Specificity	f1-score
All test samples					
f-AnoGAN-64	66	61.7	62	61	61.7
f-AnoGAN-64*	<b>85</b>	<b>75.7</b>	<b>79</b>	74.6	77.4
f-AnoGAN-256	75.4	72	54	79	62
f-AnoGAN-256*	<b>82</b>	<b>74</b>	<b>78</b>	74	75
AE-64	73.8	67.7	64	69	65.9
AE-256	75	70	58	75	64
Cracks					
f-AnoGAN-64	99	66.7	100	50	80
f-AnoGAN-64*	<b>100</b>	<b>85.7</b>	100	<b>83</b>	92
f-AnoGAN-256	99	78	100	72	87.7
f-AnoGAN-256*	<b>100</b>	<b>95</b>	100	<b>94</b>	97
AE-64	98	78	100	100	87.7
AE-256	100	95	100	94	97
Micro					
f-AnoGAN-64	63	58.7	59	59	58.9
f-AnoGAN-64*	<b>80.5</b>	<b>71.8</b>	<b>76.7</b>	70	74
f-AnoGAN-256	72.7	70	47	80	56
f-AnoGAN-256*	<b>78</b>	<b>73</b>	<b>73</b>	74	73
AE-64	71	66.5	63.7	67.9	65
AE-256	70	66	53	72	59
Finger int.					
f-AnoGAN-64	70	66	64.9	66.7	65.5
f-AnoGAN-64*	<b>84.4</b>	<b>74.8</b>	<b>81</b>	72.6	77.8
f-AnoGAN-256	77.8	74	62	79	68
f-AnoGAN-256*	<b>86</b>	<b>78</b>	<b>85</b>	75	81
AE-64	69.7	61.9	59.8	63	60.8
AE-256	75	69	63	71	66

Table 2: The results of anomaly detection at the image level. The Precision tells how accurate the classifier is when classifying a sample as defective. The recall tells how many samples have been correctly classified as defective from all defective samples. The Specificity describes how many defect-free samples have been correctly classified as defect-free samples. And the F1-score is the harmonic mean of the Precision and Recall. In all metrics, the higher the value, the better the classifier it is

eral, patch-based approaches could detect more defects, but they had more false positives cases.

With respect to the defect location results, it can be observed in fig.6 that all the models were able to properly detect the different defects. Nevertheless, the segmentation results were more refined in f-AnoGAN-256 and AE-256 models, where the images

are processed in one step. While results from these latter models were clean in the defect-free samples, and only defective areas were segmented in the defective samples, the patch-based models had several false positive cases. This is visible in the segmentation of f-AnoGAN-64 and AE-64 model of the samples in the second and last row. In the sample from

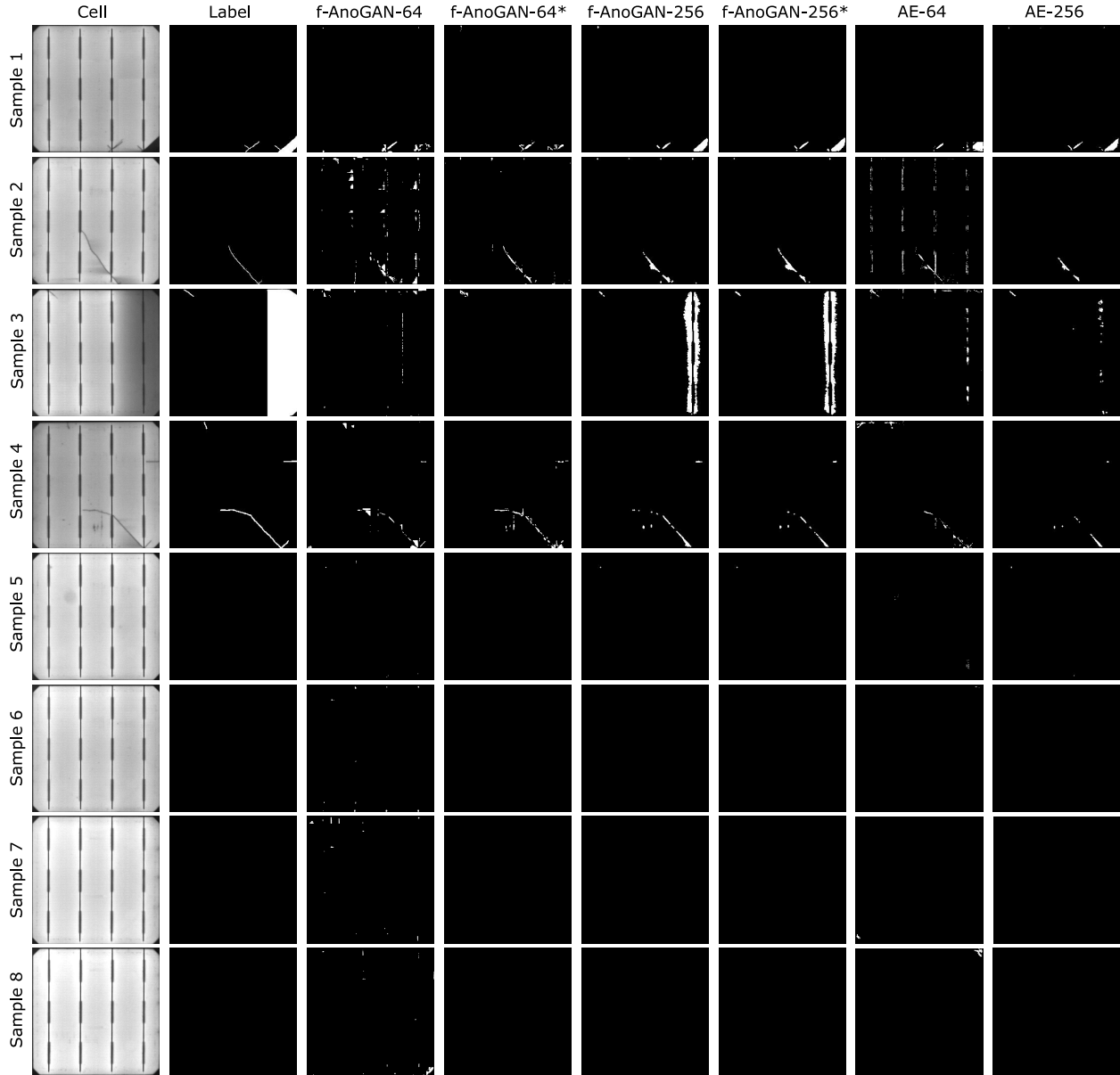


Figure 6: Defect localization results from each model

the second row, the results from patch-based models show that the buses were classified as defects. And in the sample from the last row, the corners in the image that are not part of the cell body are segmented

as defective.

Is also worth mentioning, that some type of defects that were not considered in the analysis of the quantitative results were also located. These defects are

breaks (in the cell from the first row) and bad soldering (in the cell from the third row). These types of defects were discarded for the quantitative analysis as there were just a few samples for a proper analysis. However, it is interesting to find that some methods, especially f-AnoGAN-256 and f-AnoGAN-256\*, can also locate these kinds of defects.

Regarding the time required to process the image, it was considerably reduced. The tab.3 shows that patch-based approaches required more than a second to process a cell. But with the architecture modification, this time was reduced to 0.05 seconds and 0.02 seconds per cell for f-AnoGAN-256 and AE-256, respectively.

Model	time per patch	time per image
f-AnoGAN-64		
f-AnoGAN-64*	0.02s	5.12s
f-AnoGAN-256		
f-AnoGAN-256*	-	0.05s
AE-64	0.012s	3.07s
AE-256	-	0.02s

Table 3: Time required to process a cell for each model

It can be concluded, that f-AnoGAN with the architecture modification met the specified inspection time (under 1s) with greater precision, but could not detect as many defects as the patch-based approach model.

## 5.2 Training scheme modification

In the second experiment, the training scheme was altered so the final detection rate could be improved. The results in tab.2 show that the training scheme modification had a positive impact in all the metrics after. Both f-AnoGAN-64\* and f-AnoGAN-256\* improved their the detection rate for all kinds of defects. In the case of the f-AnoGAN-64\* model, it detected more defective cells without increasing the false positives cases, i.e. precision, recall, and specificity values were all greater than with the f-AnoGAN-64 model.

In the case of f-AnoGAN-256\*, it also detected more defective cells if compared with f-AnoGAN-256 but it implied a slight increase in some false positive cases in microcrack and finger interruptions defect. This is appreciable in the value of specificity in finger interruption and microcrack types of defect, which decreased from 79 to 75 and from 80 to 74, respectively. There was no such effect in the value of the precision as the number of detected defective cells (true positives) increased notoriously. If compared with Autoencoders, they overcame their results that were worse in the previous experiment. The improvement can also be seen in the ROC curves in fig.5, where the curves of f-AnoGAN-64\* and f-AnoGAN-256\* got closer to the top-left corner that represents a perfect classifier than the other models.

Regarding the pixel level results, the modification had a positive impact on the results, especially in the case of f-AnoGAN-64. The results of f-AnoGAN-64\* model show that the previous false positives were removed in defective and defect-free samples. In the case of f-AnoGAN-256, there is not a remarkable difference in the results after the training scheme modification.

With respect to image processing time, the training scheme did not alter the network architecture or any other aspect of the network that could have an impact during the anomaly detection. Thus, f-AnoGAN-64\* and f-AnoGAN-256\* required the same time as f-AnoGAN-64 and f-AnoGAN-256 shown in tab.3.

The conclusion that can be drawn from this experiment is that the training scheme modification improved the network detection rate without any impact in the image processing time.

Overall, f-AnoGAN-64\* was the model with the best results regarding the detection rate. However, it should be taken into account that with f-AnoGAN-256\* model, where both modifications were applied, the detection rates were similar but with shorter processing time. Being this a critical requirement of an inspection system, f-AnoGAN-256\* is considered the model with the overall best results.

### 5.3 Automatic labeling

After the evaluation of the results from anomaly detection, defective samples were automatically labeled for the supervised training. The labeling was performed using f-AnoGAN-256\* model. In fig.7, some samples of from the automatic labeling are shown side by side with their corresponding manual labeling.

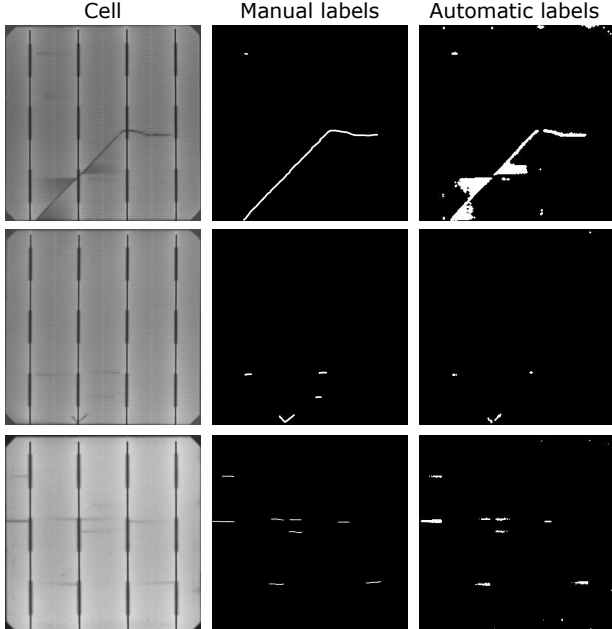


Figure 7: Manual and automatic labeling samples for different samples

In fig.8 and tab.4, the qualitative and quantitative results from training U-net with manual and automatic labels are shown. As it can be seen in fig.8, the defect localization results from the anomaly detection are improved after the supervised training.

Model	mIoU
U-net w/ manual labels	64
U-net w/ auto. labels	66

Table 4: Pixel-level results from U-net using manually created labels and automatically created labels

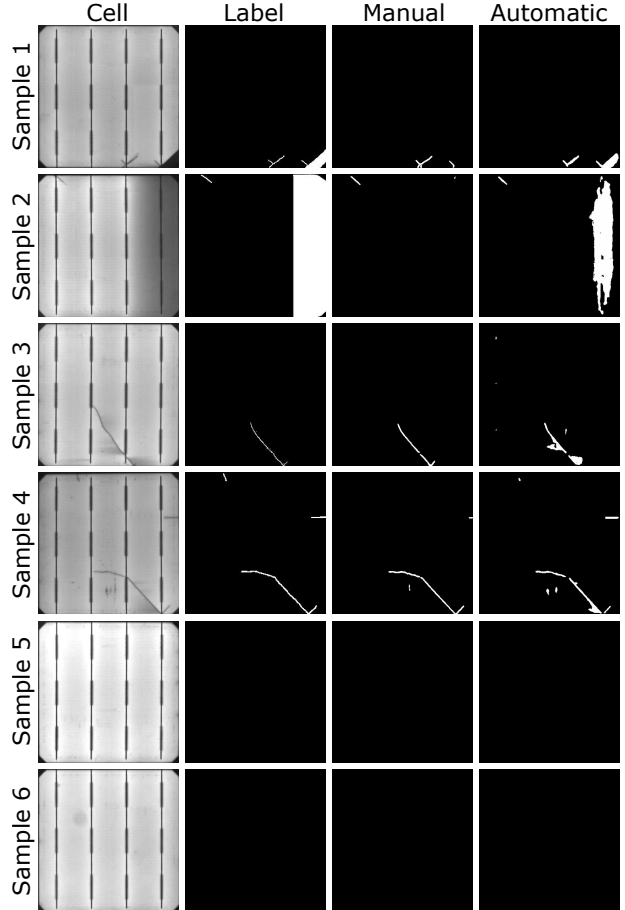


Figure 8: Results from supervised training. Manual refers to the results when using ground truth labeled by experts, and automatic refers to the results obtained when using ground truth that have been automatically with the proposed pipeline.

The automatic annotation helped to improve the final segmentation even if the samples included some false positives. For example, in the sample from the second row with manual labels, only the microcrack was segmented. But, with automatic labels, the bad soldering was also partially segmented. The same happened with the break in the cell from the first row. With manual labels, only the microcrack was detected, but with automatic labels the break was

also segmented. Moreover, certain kinds of defects that were previously detected, they were more thoroughly marked with automatic labels (e.g. sample from the fourth row). In the case of false positives, they did not experiment any noticeable increase. The ones that were segmented with manual labels, were still segmented when using automatic labels. With regards to defect-free samples, automatic labeling has no impact on the results. Defect-free samples have been kept clean with both kinds of annotations.

## 5.4 Discussion

After the analysis of the results, two aspects seemed to have great impact on the models' performance: The number of defective pixels in the images and the annotation of the areas around the defects.

Regarding the number of defective pixels in the images, the ROC curves in fig.5 and the metrics in tab.2 show that the greater the number of defective pixels, the greater detection rates were obtained. All models could detect all crack type samples, but they could not detect all samples with microcracks and finger interruptions. The cracks are defects that cover a larger area of the cells than the finger interruption or microcrack, consequently, they provide many more defective pixels to the cell. When calculating the anomaly score defined in eq.2, the residuals yield higher reconstruction error. Hence, it is easier to differentiate defective cells with crack from defect-free cells than with the other types of defects. In the case of microcracks and finger interruption, the microcracks commonly appear isolated in the cells while finger interruptions appear in groups of three or more. Due to this distribution, samples with finger interruptions present more defective pixels than the samples with microcrack. This leads to greater reconstruction error, which eases the classification between defective and defect-free cells.

Concerning the annotations, it seems that annotating dark areas around the defects helped the models in the segmentation. For example, in the first sample in fig.7 manual label does not cover the areas around the defect, whereas with automatic labeling these areas are annotated as defective. The experts did not consider these areas during the labeling as

they are not part of the defect but the consequence of the defect itself. However, these dark areas will not appear in defect-free cells. Because of that, anomaly detection network annotated them as defective areas. By considering these areas as part of the labels during the supervised training, it seems that the supervised model understood that while in manual labeling were not considered as defective, yes they were in automatic labeling. Consequently, as it can be observed in fig.8, even if the class was not included in the training, the dark area in the right that belongs to a bad soldering defect was segmented when using automatic labels and not when using manual annotations. Moreover, the segmentation of other defects, for example, the break in the first sample or the finger interruption in the fourth sample, have been more accurately segmented. This means that it was important to label not only the defect itself, but also the defective areas that are the consequence of the defects to get a better segmentation results.

## 6 Conclusions

In this work, a Generative Adversarial Network based anomaly detection approach has been proposed for the quality inspection of monocrystalline solar cells. With anomaly detection, only defect-free samples are required to obtain a model for inspection which can detect and locate defects in the cells. This feature is key for the development of a PV module inspection system as it permits having an inspection model from the very beginning stage of a new production line. There is no need to wait to have defective data and annotate them to train a model for inspection. This approach saves a lot of time and effort concerning data preparation when constructing an inspection system.

In order to apply anomaly detection for industrial inspection, a GAN proposed to detect and locate anomalies in the medical domain has been adapted. The adaptations have been two-fold: First, the architecture has been modified such that the images can be processed in a single step instead of processing them by patches. In this way, less time is required to process a cell, and therefore, the established inspec-

tion time mark (less than a second per cell) has been met. And second, the training scheme has also been modified. This modification has resulted in an improvement in the defect detection capabilities of the model.

In addition, it has been experimentally demonstrated that the results from the anomaly detection are potential pixel-wise labels that can be used in a supervised training. In the experiment, the defect localization results obtained from a model trained with expert generated labels and a model trained with automatically generated labels have been compared. The comparison has shown that using automatic labels can yield similar location results as using manual annotations, in some cases more precise.

The results from the experiments have shown a complete pipeline that can be used in the development of an inspection system for solar cells. In the first stage where there are no defective samples available, anomaly detection can be applied to detect and locate defective cells. Then, as defective samples arise, the model will annotate them. When there are enough defective cells accumulated, they will be used to train a model in a supervised manner to improve the results. In this way, the time-consuming data annotation and inspection tasks will be automated.

## 7 Acknowledgments

This research was developed as part of the Elkarteek project ENSOL 2 (KK-2020/00077) supported by the Basque Government. Jean Philippe Agerre and Jon Altube from Mondragon Assembly S. Coop. for providing us with a real industrial dataset.

## References

Akcay S, Atapour-Abarghouei A, Breckon TP (2019) Ganomaly: Semi-supervised anomaly detection via adversarial training. In: Jawahar CV, Li H, Mori G, Schindler K (eds) Computer Vision – ACCV 2018, Springer International Publishing, Cham, pp 622–637

Akram MW, Li G, Jin Y, Chen X, Zhu C, Zhao X, Khaliq A, Faheem M, Ahmad A (2019) Cnn based automatic detection of photovoltaic cell defects in electroluminescence images. *Energy* p 116319

Akram MW, Li G, Jin Y, Chen X, Zhu C, Ahmad A (2020) Automatic detection of photovoltaic module defects in infrared images with isolated and develop-model transfer deep learning. *Solar Energy* 198:175 – 186, DOI <https://doi.org/10.1016/j.solener.2020.01.055>

Anwar SA, Abdullah MZ (2014) Micro-crack detection of multicrystalline solar cells featuring an improved anisotropic diffusion filter and image segmentation technique. *EURASIP Journal on Image and Video Processing* 2014(1):15

Balzategui J, Eciolaza L, Arana-Arexolaleiba N (2020) Defect detection on polycrystalline solar cells using electroluminescence and fully convolutional neural networks. In: 2020 IEEE/SICE International Symposium on System Integration (SII), IEEE, pp 949–953

Bartler A, Mauch L, Yang B, Reuter M, Stoicescu L (2018) Automated detection of solar cell defects with deep learning. In: 26th European Signal Processing Conference, EUSIPCO 2018, Roma, Italy, September 3-7, 2018, IEEE, pp 2035–2039, DOI 10.23919/EUSIPCO.2018.8553025

BNEF FSUC (2019) global trends in renewable energy. URL <https://www.fs-unep-centre.org/global-trends-in-renewable-energy>

Chen H, Pang Y, Hu Q, Liu K (2018a) Solar cell surface defect inspection based on multispectral convolutional neural network. *Journal of Intelligent Manufacturing* DOI 10.1007/s10845-018-1458-z

Chen H, Zhao H, Han D, Yan H, Zhang X, Liu K (2018b) Robust crack defect detection in inhomogeneously textured surface of near infrared images. In: Chinese Conference on Pattern Recognition and Computer Vision (PRCV), Springer, pp 511–523

Chen H, Zhao H, Han D, Liu K (2019) Accurate and robust crack detection using steerable evidence filtering in electroluminescence images of solar cells. *Optics and Lasers in Engineering* 118:22–33

Chen H, Hu Q, Zhai B, Chen H, Liu K (2020) A robust weakly supervised learning of deep convnets for surface defect inspection. *Neural Computing and Applications* pp 1–16

Chen X, Konukoglu E (2018) Unsupervised detection of lesions in brain mri using constrained adversarial auto-encoders. In: MIDL Conference book, MIDL

Deitsch S, Christlein V, Berger S, Buerhop-Lutz C, Maier A, Gallwitz F, Riess C (2019) Automatic classification of defective photovoltaic module cells in electroluminescence images. *Solar Energy* 185:455–468

Demant M, Rein S, Haunschild J, Strauch T, Hofler H, Broisch J, Wasmer S, Sunder K, Anspach O, Brox T (2016) Inline quality rating of multicrystalline wafers based on photoluminescence images. *Progress in Photovoltaics: Research and Applications* 24(12):1533–1546, DOI 10.1002/pip.2706

Demirci M, Beşli N, Gümüşçü A (2019) Defective pv cell detection using deep transfer learning and el imaging. *Proceedings Book* p 311

Dunderdale C, Brettenny W, Clohessy C, van Dyk EE (2020) Photovoltaic defect classification through thermal infrared imaging using a machine learning approach. *Progress in Photovoltaics: Research and Applications* 28(3):177–188

Fuyuki T, Kitiyanan A (2009) Photographic diagnosis of crystalline silicon solar cells utilizing electroluminescence. *Applied Physics A* 96(1):189–196, DOI 10.1007/s00339-008-4986-0

Goodfellow I, Pouget-Abadie J, Mirza M, Xu B, Warde-Farley D, Ozair S, Courville A, Bengio Y (2014) Generative adversarial nets. In: Advances in neural information processing systems, pp 2672–2680

Gulrajani I, Ahmed F, Arjovsky M, Dumoulin V, Courville A (2017) Improved training of wasserstein gans. In: Proceedings of the 31st International Conference on Neural Information Processing Systems, Curran Associates Inc., Red Hook, NY, USA, NIPS’17, p 5769–5779

Haselmann M, Gruber DP, Tabatabai P (2018) Anomaly detection using deep learning based image completion. In: 2018 17th IEEE International Conference on Machine Learning and Applications (ICMLA), IEEE, pp 1237–1242

Hinton G, Srivastava N, Swersky K (2012) Neural networks for machine learning lecture 6a overview of mini-batch gradient descent.

IEA (2019) Renewables 2019. URL <https://www.iea.org/reports/renewables-2019>

Kignma DP, Ba J (2014) Adam: A method for stochastic optimization. *Arxiv preprint arxiv:14126980*

Ko J, Rheem J (2010) Anisotropic diffusion based micro-crack inspection in polycrystalline solar wafers. In: World Congress on Engineering 2012. July 4–6, 2012. London, UK., International Association of Engineers, vol 2188, pp 524–528

Köntges M, Kunze I, Kajari-Schröder S, Breitenmoser X, Bjørneklett B (2011) The risk of power loss in crystalline silicon based photovoltaic modules due to micro-cracks. *Solar Energy Materials and Solar Cells* 95(4):1131–1137

Liu L, Zhu Y, Rahman MRU, Zhao P, Chen H (2019) Surface defect detection of solar cells based on feature pyramid network and ga-faster-rcnn. In: 2019 2nd China Symposium on Cognitive Computing and Hybrid Intelligence (CCHI), IEEE, pp 292–297

Luo Z, Cheng S, Zheng Q (2019) Gan-based augmentation for improving cnn performance of classification of defective photovoltaic module cells in electroluminescence images. In: IOP Conference Series: Earth and Environmental Science, IOP Publishing, vol 354, p 012106

Mayr M, Hoffmann M, Maier A, Christlein V (2019) Weakly supervised segmentation of cracks on solar cells using normalized lp norm. In: 2019 IEEE International Conference on Image Processing (ICIP), pp 1885–1889, DOI 10.1109/ICIP.2019.8803116

Nos O, Favre W, Jay F, Ozanne F, Valla A, Alvarez J, Muñoz D, Ribeyron P (2016) Quality control method based on photoluminescence imaging for the performance prediction of c-si/a-si: H heterojunction solar cells in industrial production lines. *Solar Energy Materials and Solar Cells* 144:210–220

Pierdicca R, Malinverni E, Piccinini F, Paolanti M, Felicetti A, Zingaretti P (2018) Deep convolutional neural network for automatic detection of damaged photovoltaic cells. *International Archives of the Photogrammetry, Remote Sensing & Spatial Information Sciences* 42(2)

Qian X, Li J, Cao J, Wu Y, Wang W (2020a) Micro-cracks detection of solar cells surface via combining short-term and long-term deep features. *Neural Networks*

Qian X, Li J, Zhang J, Zhang W, Yue W, Wu QE, Zhang H, Wu Y, Wang W (2020b) Micro-crack detection of solar cell based on adaptive deep features and visual saliency. *Sensor Review*

Rahman MRU, Chen H, Xi W (2019) U-net based defects inspection in photovoltaic electroluminescence images. In: 2019 IEEE International Conference on Big Knowledge (ICBK), IEEE, pp 215–220

Rodriguez A, Gonzalez C, Fernandez A, Rodriguez F, Delgado T, Bellman M (2020) Automatic solar cell diagnosis and treatment. *Journal of Intelligent Manufacturing* pp 1–10

Ronneberger O, Fischer P, Brox T (2015) U-net: Convolutional networks for biomedical image segmentation. *CoRR* abs/1505.04597, URL <http://arxiv.org/abs/1505.04597>, 1505.04597

Schlegl T, Seeböck P, Waldstein SM, Langs G, Schmidt-Erfurth U (2019) f-anogan: Fast unsupervised anomaly detection with generative adversarial networks. *Medical image analysis* 54:30–44

Staar B, Lütjen M, Freitag M (2019) Anomaly detection with convolutional neural networks for industrial surface inspection. *Procedia CIRP* 79:484–489

Su B, Chen H, Zhu Y, Liu W, Liu K (2019) Classification of manufacturing defects in multicrystalline solar cells with novel feature descriptor. *IEEE Transactions on Instrumentation and Measurement* 68(12):4675–4688

Sun M, Lv S, Zhao X, Li R, Zhang W, Zhang X (2017) Defect detection of photovoltaic modules based on convolutional neural network. In: International Conference on Machine Learning and Intelligent Communications, Springer, pp 122–132

Tang W, Yang Q, Xiong K, Yan W (2020) Deep learning based automatic defect identification of photovoltaic module using electroluminescence images. *Solar Energy* 201:453–460

Tsai D, Wu S, Chiu W (2013) Defect detection in solar modules using ica basis images. *IEEE Transactions on Industrial Informatics* 9(1):122–131, DOI 10.1109/TII.2012.2209663

Tsai DM, Chang CC, Chao SM (2010) Micro-crack inspection in heterogeneously textured solar wafers using anisotropic diffusion. *Image and Vision Computing* 28(3):491–501

Tsai DM, Wu SC, Li WC (2012) Defect detection of solar cells in electroluminescence images using fourier image reconstruction. *Solar Energy Materials and Solar Cells* 99:250–262

Tsai DM, Li GN, Li WC, Chiu WY (2015) Defect detection in multi-crystal solar cells using clustering with uniformity measures. *Advanced Engineering Informatics* 29(3):419–430

Vaněk J, Repko I, Klima J (2016) Automation capabilities of solar modules defect detection by thermography. *ECS Transactions* 74(1):293–303

Wang J, Yang Z, Zhang J, Zhang Q, Chien WTK (2019) Adabalgan: An improved generative adversarial network with imbalanced learning for wafer defective pattern recognition. *IEEE Transactions on Semiconductor Manufacturing* 32(3):310–319

Ying Z, Li M, Tong W, Haiyong C (2018) Automatic detection of photovoltaic module cells using multi-channel convolutional neural network. In: 2018 Chinese Automation Congress (CAC), IEEE, pp 3571–3576

Zhang X, Sun H, Zhou Y, Xi J, Li M (2013) A novel method for surface defect detection of photovoltaic module based on independent component analysis. *Mathematical Problems in Engineering* 2013

Zhang X, Hao Y, Shangguan H, Zhang P, Wang A (2020) Detection of surface defects on solar cells by fusing multi-channel convolution neural networks. *Infrared Physics & Technology* p 103334